Evaluation of chemical and structural homogeneity in single particles of Li_{1-x}Ni_{0.33}Mn_{0.33}Co_{0.33}O₂

Authors:

William J. Judge (wjudge2@uic.edu)1, Brian M. May (brianmay19@gmail.com)1,

Khagesh Kumar (kkumar22@uic.edu)¹, Mark F. Wolfman (wolfman@anl.gov)^{1,2},

David A. Shapiro(dashapiro@lbl.gov)3, Zhonghou Cai (cai@anl.gov)2,

Martin V. Holt (mvholt@anl.gov)², Jordi Cabana* (jcabana@uic.edu – phone: (312) 355-4309)¹

1. Department of Chemistry, University of Illinois Chicago, 1200 W Harrison St, Chicago, IL USA 60607

2. Advanced Photon Source, Argonne National Laboratory, 9700 S Cass Ave, Lemont, IL USA 60439

3. Advanced Light Source, Lawrence Berkeley National Laboratory, 1 Cyclotron Rd, Berkeley, CA USA 94720

Abstract: Identifying irreversible phenomena at single particles of battery cathode materials is an

important step to understanding degradation pathways upon cycling. LiNi_{0.33}Mn_{0.33}Co_{0.33}O₂

(LiNMC(111)) single particles of size 200 x 300 nm were studied before and after cycling using Scanning

X-Ray Diffraction Microscopy (SXDM) and ptychographic microscopy. With resolutions of 30nm and

5nm, respectively, it was possible to map the inter-particle (003) reflection and nickel oxidation state

changes at different states of charge. While the compositions measured by the c lattice parameter

from SXDM were found to be homogeneous, mapping at higher resolution using ptychography

revealed that Ni oxidation states decrease sharply 0-25nm from the edge, then trail into a steady

oxidation state towards the interior of the particle. Within the 30nm length scale we conclude

LiNi_{0.33}Mn_{0.33}Co_{0.33}O₂ single particles are highly structurally reversible.

Keywords: nano-scale, cathode, LiNMC, SXDM, ptychography

1

1.1 Introduction

Over the past two decades, significant effort has been placed on improving the materials used in *Li**-ion batteries. These improvements have targeted increased capacity, power, and lifetime^{1–3}, and were informed by increased insight into the reactions occurring at the level of individual particles^{4,5}. To fully understand the inner workings of single particles of *Li**-ion cathodes, multiple instrumental modalities must be coupled in order to obtain a complete picture of the consequences of irreversibility and, thus, degradation of structure and chemistry. Common degradation mechanisms involve, but are not limited to, cathode-electrolyte side reactions⁶, competing structural transformations^{6,7}, and delamination due to mechanical strain⁸. Since individual cathode particles often have sizes at the nano-scale^{9,10}, understanding material degradation within them demands techniques that can resolve chemical phenomena at high spatial resolution¹¹. The model system chosen was LiNi_{0.33}Mn_{0.33}Co_{0.33}O₂ for its balance of performance, power delivery, and abundance of secondary-bulk material studies in the literature^{12–15}. To obtain a more comprehensive knowledge base for these nanomaterials, we must choose experimental techniques well suited for the task.

To study the evolution of nano-scale phase changes in materials it follows that an appropriate instrument must be able to image chemical state at comparatively higher spatial resolutions. Electron microscopy can achieve highly desirable chemical and spatial resolutions¹⁶, but at the cost of physically thin sample requirements (<100nm) and the potential for significant beam damage to the sample due to the high energy of the probe beam¹⁷. Therefore, complementary techniques are welcome that can offer means to bypass these shortcomings while providing sufficient chemical and spatial insight. One technique is X-ray absorption spectroscopy (XAS) coupled with ptychographic imaging that can achieve 5nm resolution of redox states. Pairing ptychographic techniques with Bragg diffraction

imaging techniques, such as Scanning X-ray Diffraction Microscopy (SXDM), then allows one to determine crystallographic strain for a given material¹⁸. Here, we apply SXDM and ptychography to probe redox and structural homogeneity within well-defined particles of LiNi_{0.33}Mn_{0.33}Co_{0.33}O₂ upon Li deintercalation and reintercalation.

1.2 Materials and Methods

1.2.1 Sample Preparation

LiNi_{0.33}Mn_{0.33}Co_{0.33}O₂ platelets were synthesized following a two-step process detailed for $LiNi_{0.8}Co_{0.15}Al_{0.05}O_2$ in Wolfman et al.⁹, May et al.¹⁹, and Zhang et al.²⁰. First, Ni(NO₃)₂· 6H₂O, Co(NO₃)₂· 6H₂O, Mn(NO₃)₂· 4H₂O were first mixed in water at stoichiometric ratios, followed by addition of NaOH using a molar ratio of 1:2, in a total of 70 mL of solution^{9,19,20}. The mixture was transferred in a Teflon-lined stainless vessel, which was sealed and treated at 160 °C for 18hr to produce a hydroxide precursor hydrothermally. The precursor was washed, dried, mixed with a stoichiometric amount of LiOH · H₂O and subsequently calcined at 800 °C for 1hr to produce the final oxide. The decreased calcination time ensured the particles had the crystal structure of interest, while not being too thick for ptychographic experiments and allowed for faster orientation alignment in Scanning X-ray Diffraction Microscopy experiments.

Prior to the SXDM measurements, samples were characterized by powder X-ray diffraction (XRD) using a Bruker D8 Advance with Cu K α (1.54Å) radiation. Particles were dispersed in a copper grid with alphanumeric markings for analysis by electron microscopy and to locate such suitable particles for analysis by SXDM. Candidate particles were identified based on size, morphology, and orientation, using a JEOL JSM-6320F field emission scanning electron microscope (SEM) at a working distance of 8

mm and electron beam energy of 3.0 kV. Transmission electron microscopy was also used to determine particle morphologies, where we used an accelerating voltage of 300 kV on a JEOL JEM-3010.

To produce samples at different stages of the oxidation reaction, the LiNi_{0.33}Mn_{0.33}Co_{0.33}O₂ particles underwent electrochemical cycling. The powder was mixed with carbon black and polyvinylidene fluoride (PVDF) in a 8:1:1 weight ratio in N-methyl-2-pyrrolidone (NMP) and coated onto an Al foil current collector and dried. 2032-type coin cells were constructed using Li metal as a counter electrode. The electrolyte chosen was one of 1M LiPF₆ in a 1:1 ratio of ethylene carbonate: dimethyl carbonate. 2032-type cells were charged galvanostatically with cutoff potentials of 2.7V-4.75V at a rate of C/10.

1.2.2 Scanning X-ray Diffraction Microscopy

Experimental procedures are similar to those found in May et al. 21 . The key differences between methods are that while May et al. used the Fe X-ray fluorescence to locate particles, our approach used the Ni X-ray fluorescence signals $K\alpha$ emission line of 7.48 KeV. Also, instead of aligning on the (020) diffraction signal position, our method aligned the detector on the (003) reflection. The (003) reflection is at an approximate angle of 16.70° 20 at a wavelength of 1.377Å and was chosen for its direct relationship with the c-lattice parameter and synchronous relationship with the a-lattice parameter²². The uncertainty in the position of the annulus has been shown to be stable with an error rate of 0.657 microrads $(3.76 \times 10^{-5} \text{ degrees})^{18}$. Therefore, the error in the measured angle positions of the diffraction annulus, in this manuscript, should be negligible.

1.2.3 Data Analysis

1.2.3.1 Region of Interest Map

For each sample angle selected the X-ray beam was rastered across the field of view. At each beam position the diffraction pattern was summed to a single value and placed into a corresponding mapping position within an image matrix. This process was repeated for every beam raster position. Once this Region of Interest Map was created for all sample angles, Ni X-ray fluorescence data was used to align scans, and summed together to represent the field of view selected.

1.2.3.2 Summed Diffraction Plot

For each sample angle selected, a set amount of beam raster positions needed to complete the desired maps were determined. Diffraction patterns were taken at each of these raster positions. All diffraction images for all raster positions in the set of sample angles were summed together to create a single Summed 2D X-ray Diffraction Plot for the field of view in question.

1.2.3.3 Centroid Maps

For each $2\theta/\chi$ precursor matrix position the 2D diffraction pattern was summed in the $\chi/2\theta$ axes, which produced a plot of intensity vs $2\theta/\chi$. Hot and dead pixel subtraction methods were implemented using a selective median blur. The centroid of the data was taken through a center of mass equation. The center of mass was then stored into an image array for each beam raster position and plotted. This result was the creation of the Centroid Maps for their respective axes.

1.2.4 Ptychography

Ptychography was performed using the COSMIC ptychographic microscope on beamline 7.0.1.2 at the Advanced Light Source. Identical sample preparation, such as material drop casting on copper TEM

grids and glovebox usage, found in Wolfman et al.⁹ was implemented. Once samples were imaged through TEM and placed into beamline 7.0.1.2. The outer zone plate width was 45 nm while the scanning step size was 40nm. Using SHARP²³, reconstructions and data analysis were also identical to Wolfman et al.⁹, however the minimal spatial resolution achieved was ~5 nm.

1.2.5 SXDM Data Analysis Software

Computational analysis of Methods 1.2.3.1-1.2.3.3 were carried out using the sxdm python $module^{24}$.

1.3 Results & Discussion

1.3.1 Pristine LiNi_{0.33}Mn_{0.33}Co_{0.33}O₂

LiNi_{0.33}Mn_{0.33}Co_{0.33}O₂ was synthesized through a hydrothermal method (see Methods 1.2.1). Transmission Electron Microscopy (TEM) confirmed the platelet morphology, with thickness below 100 nm (based upon degree of transparency), as shown in the representative image of Figure S2a. However, the in-plane (z) dimensions were not uniform from particle to particle. Scanning Electron Microscopy (SEM) revealed that the lateral dimensions ranged from 100 nm * 100 nm to 600 nm * 600 nm (Figure S2b). All reflections in the pattern of powder X-ray diffraction (PXRD, Figure S3) matched the expected layered structure, with no discernible impurities. Of particular importance is the (003) reflection peak in the diffraction pattern. Not only is it the strongest signal, but its position tracks the lithium concentration in these layered systems. A modified Li concentration curve versus clattice parameter plot, found in Yoon et al. 25, is shown in Figure S1, and was used as calibration curve to extract average Li concentrations from lattice parameters extracted from SXDM measurements. A Pawley fit (Figure S3) with space group $R\overline{3}m^{26}$ yielded cell parameters a = 2.866Å and c = 14.18Å, which agree with literature values a = 2.866Å and a = 14.18Å, which agree with literature values a = 2.866Å

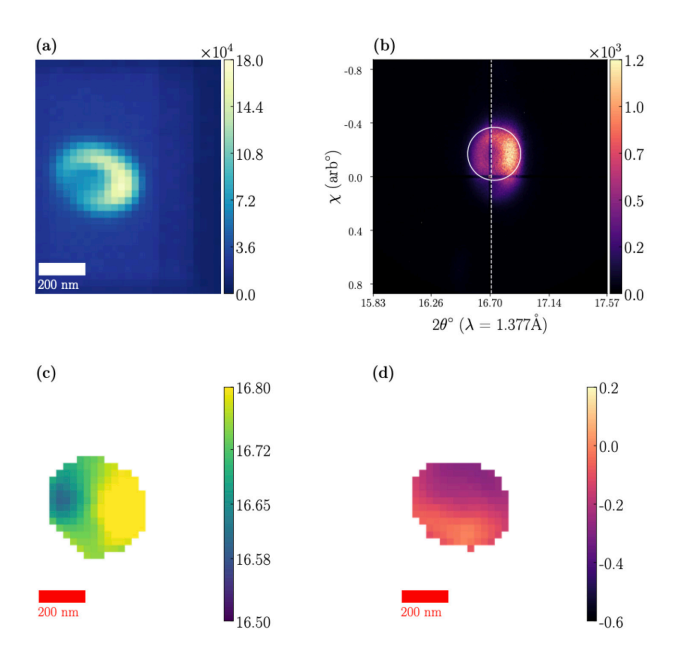


Figure 1. Single particle of pristine $Li_{1.00}Ni_{0.33}Mn_{0.33}Co_{0.33}O_2$, taken at (003) reflection. Plot (a) represents the Region of Interest Map. (b) represents the Summed 2D Diffraction Pattern. The dotted white line denotes the assigned center of the sample signal (16.708°), while the white circle denotes the shape and diameter of the beam annulus on the sample, thus denoting the instrumental broadening. (c) and (d) display the 2θ and χ Centroid Maps, respectively. The complete description of the figure can be found in the following section.

For the analysis by SXDM, samples were aligned with the detector to probe the intensity around the (003) reflection for its particular importance. Not only is it the strongest signal, but its position tracks the lithium concentration in these layered systems with high sensitivity. A modified Li concentration curve versus c-lattice parameter plot, found in Yoon et al.²⁵, is shown in Figure S1, and will be used as calibration curve to interpolate average Li concentrations from lattice parameters extracted from SXDM measurements. Figure 1a-d presents the data collected for pristine

LiNi_{0.33}Mn_{0.33}Co_{0.33}O₂. The Region of Interest (ROI) map (Figure 1a) represents the total diffraction intensity, across all collected sample angles, per mapping position within the field of view (FOV).

This map delineates a single particle measuring 250nm x 250nm. Shadowing effects led to a circular dip in total diffraction intensity at the center of the crystal. Figure S4 shows the Ni fluorescence signal from the same FOV, revealing that there were other particles present which did not meet the Bragg condition and, thus, did not diffract in these conditions. Since there is no apparent circular dip in the fluorescence intensity, it can be concluded that the drop in total diffraction intensity was not induced by an unfocused beam. Instead, we posit that this loss of signal was due to surface roughness and particle agglomeration based on the microstructure revealed in TEM and SEM images (Figure S2 a-b).

To map the crystal structure of the pristine particle, a similar protocol to May et al. was used²¹. Each X-Y- θ mapping diffraction pattern was summed to build a representative two-dimensional (2D) (2 θ vs. χ) pattern²¹. Figure 1b represents this diffraction signal integrated for the entire crystal. The summation is used to analyze the average structural features within the object. The white dotted circle (diameter of $0.396^{\circ} = \Delta_{Instrument}$) represents the instrumental broadening estimated based on the shape and position of the incoming beam. The small proportion of signal outside the expected dispersion of signal can be attributed to X-ray scattering at the edges of the particle. The clear circular shape, or annulus, of the aggregate signal indicates that the particle was single crystalline¹⁸. However, it is worth noting the existence of a slight asymmetry in the intensity of the diffraction around the annulus, toward higher angles, which was again ascribed to shadowing due to surface morphological roughness. The white dotted line at $2\theta = 16.708^{\circ}$ in Figure 1b represents the assigned 2θ position for the center of the diffraction annulus. Using Bragg's law with the incoming wavelength, λ =1.377Å, and

the Miller index of the observed reflection, a value of the cell parameter was produced, c = 14.217Å, in agreement with the literature^{27,28}. All assignments of summed 2D diffraction 2θ positions were chosen at the center of their respective diffraction annuli.

To help analyze the non-trivial integrated 2D diffraction pattern signal further, our analysis followed both the relative movements of the centroid position and the angular broadening of the signal, $2\theta_{Pristine}$, in comparison with the expected instrumental value, $\Delta_{Instrument}$ (0.396°). In terms of 2 θ , any 2 θ larger than $\Delta_{Instrument}$ immediately indicates more than one crystal lattice spacings in the field of view. Values below this threshold require individual inspection of the patterns to ensure that any changes in centroid are due to a solid movement of the annulus, as opposed to changes in the distribution of intensity around an otherwise static annulus.

Figure 1c maps the position of the centroid along 2θ within the particle studied. It shows an apparent shift in position from left to right on the particle. Upon close inspection of the raw diffraction data (Video 1(https://tinyurl.com/2p8a62rk,https://github.com/WilliamJudge94/thesis_videos)) the signal envelope never leaves the region within the $\Delta 2\theta_{Pristine}$ annulus for an invariant 2θ position (16.708°). Instead, the distribution of relative intensities of signal within the annulus changes from left to right on the particle. The irregular distribution of the signal induces an artificial shift in the estimation of the centroid with the algorithm used here (See Methods section number 1.2.3.3). All in all, from the visual inspection of Video 1, it is clear that the annulus actually remains in the same position throughout the particle. The same effects were observed in the spatial distribution of χ centroid positions (Figure 1d with a standardized χ color scale of 0.80°). In this case, the variations in distribution of relative intensity within an invariant annulus across mapping positions induced an apparent shift in values from top to bottom of the particle. Therefore, it can be concluded that all 2θ

and χ centroids can be treated as a single, static value across the particle, consistent with the single crystalline character of the summed diffraction signal of the particle.

A second field of view was measured for the pristine material (Figure 2). Analysis of the second pristine field of view ROI map, 2θ centroid map, and χ centroid map resulted in similar conclusions (Figure 1). However, the annulus center was positioned at a lower 2θ value in this FOV, 16.65° , which corresponds to c = 14.271 Å. The variation in cell parameter between particles was ascribed to variations in the defect concentration between particles. Literature has shown that crystallographic site exchange between Li and Ni is common for LiNi_{0.33}Mn_{0.33}Co_{0.33}O₂. The presence of Ni in the Li increases the c lattice parameter^{22,29} More specifically, analysis of powder XRD by Fujii et al. showed that the c lattice parameter increases from 14.23Å to 14.26Å as the percentage of exchange doubles from 2.79% to 4.88%.²² Ensemble averaging of PXRD signals possibly causes that variations outside this single value could be detected when looking at cell parameters in single particles. The values of c parameter observed here (Figure 1, Figure 2) are within the range reported by Fujii et al., consistent with local variations in Li/Ni site exchange.

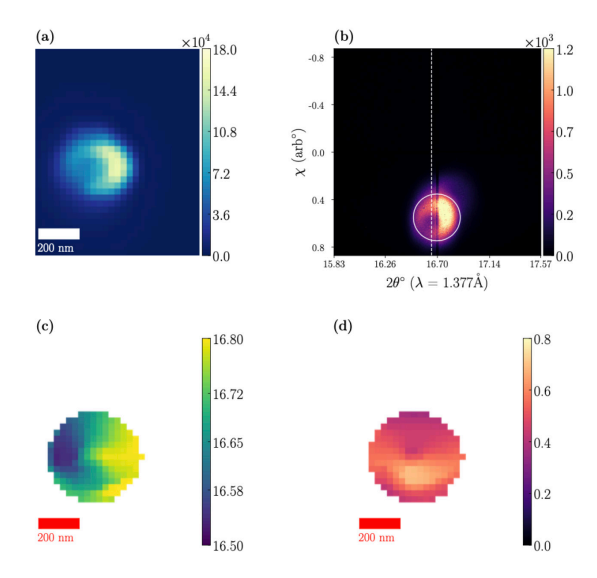


Figure 2. Representations of a second particle in the pristine state. Plot (a) is a Region of Interest Map. (b) is a Summed Diffraction Map. The dashed white line represents an annuli 2θ value of 16.65° which is equal to a c-lattice spacing of 14.271 Å. The red and white circles denote the shape and diameter of the beam annulus on the sample, thus denoting the instrumental broadening. (c) and (d) display the 2θ (delta = 0.280°) and χ (delta = 0.215°) Centroid Maps, respectively.

1.3.2 Charged LiNi_{0.33}Mn_{0.33}Co_{0.33}O₂

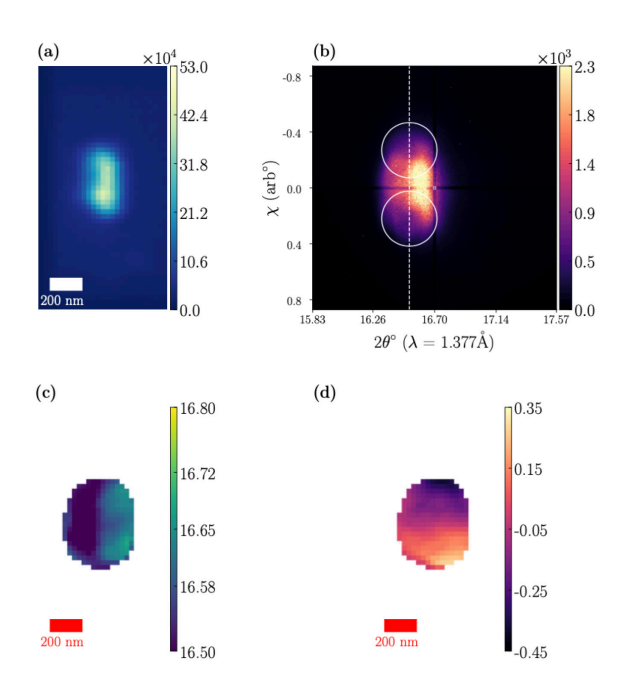


Figure 3. Field of view for charged $Li_{0.32}Ni_{0.33}Mn_{0.33}Co_{0.33}O_2$, taken at the (003) reflection. Plot (a) is a Region of Interest Map. (b) is a Summed Diffraction Map. The dashed white line represents a 2θ value of 16.52° which is equal to a c-lattice spacing of 14.377 Å. The white circle denotes the shape and diameter of the beam annulus on the sample, thus denoting the instrumental broadening. (c) and (d) display the 2θ and χ Centroid Maps, respectively.

Identical analyses were performed for a particle recovered from a sample after a charge to 4.75V (Figure 3). An example cycling profile can be found in Figure S5. The calculated capacity for the cell was 271 mAh/g, corresponding to an average lithium value of Li_{0.03}Ni_{0.33}Mn_{0.33}Co_{0.33}O₂, assuming 100% faradaic efficiency. It was necessary to determine minimal particle morphology changes during cycling. Minimal changes in morphologies were confirmed by comparing the ROI mapping (Figure 3a) and scanning electron microscopy (Figure S2b). However, removing lithium from the structure increased the complexity of the diffraction signals. More than one single crystalline domain fulfilled the Bragg

condition in this ROI, as the signal was found to be a superposition of multiple annuli (Figure 3b), at least two of which could be identified using instrumental broadening circles set at two different χ values. This feature suggests that two particles were probed. Both annuli highlighted in the figure were centered around a single 2θ value of 16.52° . This value corresponds to a c lattice spacing of 14.377Å, which, according to reference data for LixNi_{0.33}Mn_{0.33}Co_{0.33}O₂ in the literature, corresponds to Li_{0.32}Ni_{0.33}Mn_{0.33}Co_{0.33}O₂ (Figure S1). There was signal spreading between these two annuli, outside the expected instrumental broadening shown by the white dotted circles in Figure 3b. It represented additional overlapping annuli; some remnant intensity appeared at slightly lower 2θ , suggesting some heterogeneity between the two particles in the FOV. In any case, comparison of the capacity of the electrode and the actual composition estimated by SXDM reveals the existence of deviations from 100% faradaic efficiency, as expected from the high cutoff potential.

As in the pristine particles, analysis of the gradient of 2θ centroids (Figure 3c) revealed variations in the distribution of intensity within an otherwise static annulus for the signals that could be resolved (Video2 (https://tinyurl.com/4vu2z4uj, https://github.com/WilliamJudge94/thesis_videos)). The gradient observed in the 2θ centroid position extracted from these nontrivial signals did not correspond to any variation in cell parameter outside the value of 14.377Å within an individual single crystal. The χ centroid (Figure 3d) showed a different trend. The calculated $\Delta\chi_{Charged}$ was determined to be 0.554. Since $\Delta\chi_{Charged}$ is larger than the expected Δ Instrument, this validated at least two different, misaligned single crystalline domains in the FOV. For two domains to exist in a FOV there either must be two misaligned crystals or interparticle domain misalignment. Due to high agglomeration found during SEM (Figure S2b) and high localization of diffraction signals found in the ROI (Figure 3a), it is more plausible for the two χ domains to be caused by two separate particles that had slightly different

orientation on the substrate used for imaging. Interestingly, these two particles not only had the same chemical state, but they were chemically homogeneous and retained a very high crystallinity, comparable to the pristine state.

Studies have shown a correlation between structural changes of Li₈Ni_{0.33}Mn_{0.33}Co_{0.33}O₂ materials and the Ni oxidation state⁹. To further interrogate possible structural heterogeneities in charged Li_{0.32}Ni_{0.33}Mn_{0.33}Co_{0.33}O₂, chemical ptychographic analysis was carried out to acquire Ni L_3 -edge X-ray Absorption Spectroscopy (XAS) with a spatial resolution of 5nm. The formal oxidation state of Ni in pristine LiNi_{0.33}Mn_{0.33}Co_{0.33}O₂ starts at a Ni^{2+} state then transitions to Ni^{3+} state upon charge^{9,30}. The Ni^{2+} L_3 -edge is dominated by a peak at 856 eV, which gives way to another at 858 eV upon oxidation^{9,30}. During elevated sates of charge (>4.5V) the 858 eV peak has been shown to shift towards higher energies^{9,30}. This knowledge was used to maximize spectral resolution with a minimum of data collection by collecting ptychographic maps at 856.40eV, 858.15 eV, and 858.67 eV. Calculated ratios of data collected at 856.40 eV, 858.15 eV, and 858.67 eV were to be used to identify the dominant $Ni^{2+}L_3$ -edge features, as well as any high energy peak shift found during elevated states of charge. The mean optical depth for the FOV selected for imaging can be seen in Figure S6. A white bounding box was placed to identify the region where a single, reasonably unobstructed particle was found. This cropped field of view was used to map potential Ni oxidation states within an individual nanoplatelet.

Maps were generated by plotting the ratio of relative intensity at three separate energies (856.40 eV, 858.15 eV, and 858.67 eV) along the Ni L_3 -edge (Figure 4). A higher relative intensity at 856.40 eV was indicative of the presence of more reduced Ni, whereas the highest oxidation would maximize intensity at 858.67 eV. It can be seen that domains with the highest concentration of reduced Ni exist

around the edge of the particle, whereas spectral intensity at higher energy was found in the interior, with the center appearing to be the most oxidized, as shown by the increased relative intensity at 858.67 eV.

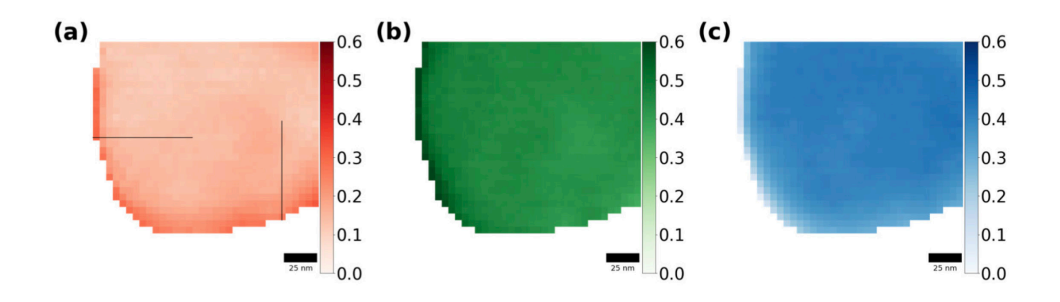
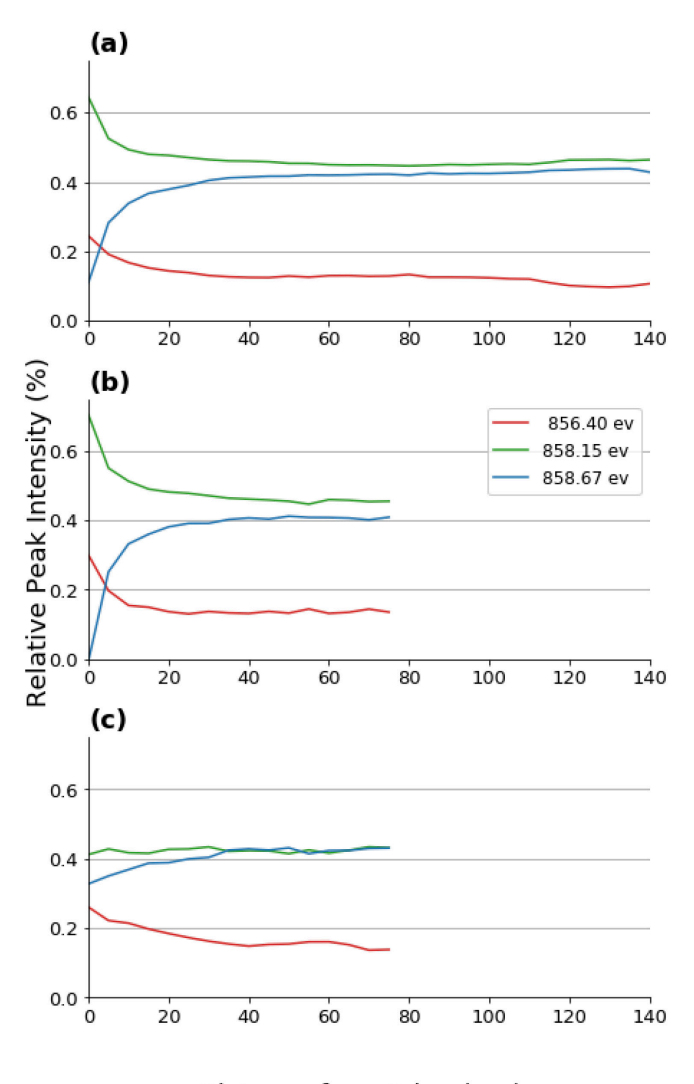


Figure 4. Ni L_3 -edge intensity ratio maps for Li_xNi_{0.33}Mn_{0.33}Co_{0.33}O₂ charged to 4.75V at a rate of C/10. a) Peak intensity ratio for 856.40eV (red). b) Peak intensity ratio for 858.15 eV (green). c) Peak intensity ratio for 858.67 eV (blue). Vertical and horizontal line scan indicators were only placed on a) to minimize the obstruction of data.

A more detailed look at the Ni redox states can be achieved by comparing relative intensity ratios of mean spectra based on distance from the edge (Figure 5a) to individual line scans from the particles edge (Figure 5b, c). Through this comparison it is shown that the signal gradient is greatest from 0-20nm from the edge of the particle. While a steady state is achieved at 45-50 nm from the edge. Reduced Ni species, indicated by an elevated 856.40 eV ratio, has greater abundance on the edge in every data scan presented (Figure 5a, b, c). Intensity ratio trends for *mean spectra based on distance* from the edge (Figure 5a) and the horizontal line scan (Figure 5b) are identical and indicate a gradient of oxidation states with a high energy peak shift towards higher energies. Similar spectral trends of these highly oxidized Ni species have also been reported by Wolfman et al.⁹ for LiNi_{0.8}Co_{0.15}Al_{0.05}O₂ materials. The vertical line scan (Figure 5c) indicates a more subtle change that is synonymous with a slight gradient of oxidation states with constant Ni²⁺L₃-edge peak positions. These metrics indicate a

chemical state heterogeneity within the charged Li_xNi_{0.33}Mn_{0.33}Co_{0.33}O₂ material depending on which side of the material one was examining.^{31,32} The origins of such transition metal gradients have been reported in the literature. These consist of non-uniform Li transport limitations³³, irreversible domain transitions to rock-salt structures upon subsequent discharge events (causing poor Li conductivity), and thickening of this rock-salt/spinel layer preventing complete oxidation of deep, pristine layered structure material.⁹



Distance from Edge (nm)

Figure 5. Intensity ratios for signal produced at 856.40 eV (red), 858.15 eV (green), and 858.67 eV (blue) for the a) mean spectrum based on distance from the particle edge, b) horizontal black line in Figure 4a, c) vertical black line in Figure 4a.

1.3.3 Discharged Li_xNi_{0.33}Mn_{0.33}Co_{0.33}O₂

Lastly, samples were analyzed after a full cycle between 4.75V and 2.7V (Figure 6). Region of Interest mapping (Figure 6a) and scanning electron microscopy (Figure S2b) again confirmed the overall morphology was not severely altered. The ROI diffraction areas consisted of ~150 by ~150 nm objects, which were clearly defined and separated from one another. Two clear annuli were captured in the measurement, both falling within the expected instrumental broadening (see circles in Figure 6b) and having comparable distributions of intensity around their perimeter. Relithiation shifted the diffraction signals back toward values closer to the pristine state. One of the annuli was positioned at a 2θ value of 16.63° (red line in Figure 6a), whereas

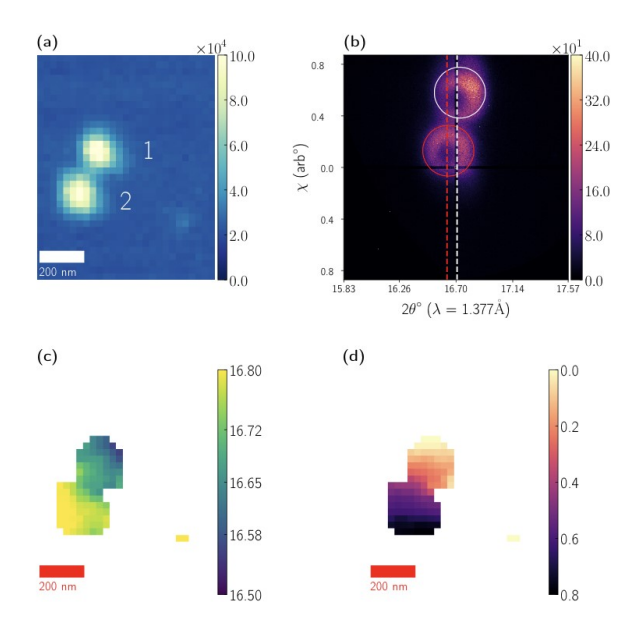


Figure 6. Multi-particle field of view for charged-discharged $Li_xNi_{0.33}Mn_{0.33}Co_{0.33}O_2$, taken at (003) reflection. Plot (a) is a Region of Interest Map. (b) is a Summed Diffraction Map. The dashed red line represents an annulus 2θ value of 16.63° which is equal to a (003) spacing of 14.283 Å. The dashed white line represents an annuli 2θ value of 16.708° which is equal to a (003) spacing of 14.217 Å. The red and white circles denote the shape and diameter of the beam annulus on the sample, thus denoting the instrumental broadening. (c) and (d) display the 2θ and χ Centroid Maps, respectively.

the second was at 16.708° (white line). These values correspond to c = 14.283 and 14.217Å), respectively. The latter value was the same as the pristine state. Using the same calibration curve to extract Li concentrations resulted in a composition of $\text{Li}_{0.83}\text{Ni}_{0.33}\text{Mn}_{0.33}\text{Co}_{0.33}\text{O}_2$ for the signal at a higher c parameter than pristine.

Analysis of discharged material (Figure 6c) shows identical trends to those found in the pristine material (Figure 1c). After close inspection of the raw diffraction data (Video 3 (https://tinyurl.com/murvtpcc,https://github.com/WilliamJudge94/thesis_videos)), each diffraction signal envelope never leaves its respective $2\theta_{Discharged}$ or $\Delta\chi_{Discharged}$ annulus for an invariant $2\theta/\chi$

position. Therefore, it can be concluded that all 2θ and χ centroids, for each individual annuli, can be treated as a single, static value across the particle they originate from. This is consistent with each particle, in the FOV, containing a single crystalline character of the summed diffraction signal of the particle. It is to be noted that each static 2θ and χ position for particles 1 and 2 are independent from one another, resulting in each particle having a uniquely uniform lattice positioning of 14.283Å and 14.217Å and a uniquely uniform crystal domain.

1.4 Conclusion

The data provided through SXDM for Li_{1.00}Ni_{0.33}Mn_{0.33}Co_{0.33}O₂ shows structural/chemical homogeneity with a spatial resolution of 30 nm. While there is incipient evidence of diffraction heterogeneity between particles in the pristine and discharged state, the spatial resolution of SXDM did not uncover sample heterogeneity within particles. However, ptychographic analysis, which could reach a resolution of 5 nm, revealed that charged particles had a gradient of Ni oxidation states within 25 nm from the surface, despite appearing single crystalline in SXDM. Overall, the results probe the reversibility in the first cycle at C/10 from 2.7V - 4.75V, particularly that the particles remain single crystalline throughout this process. While further work is needed to view the structural and chemical changes upon subsequent cycles of the material, the use of SXDM and chemical ptychography have proved to be useful in the first cycle characterization of nano-Li_{1.00}Ni_{0.33}Mn_{0.33}Co_{0.33}O₂. Follow-up work should also target the challenges of throughput that remain with SXDM today, where only particles that meet the Bragg condition can be imaged. The unique insight provided by SXDM compared to other X-ray imaging techniques should motivate further methodological advances.

1.5 Supporting Information

Supplemental Materials for this manuscript include figures describing the calibration of cell parameters versus Li concentration calibration, electron microscopy images, analysis by powder XRD of the pristine material, X-ray fluorescence mapping images from SXDM experiments, electrochemical curves, and ptychographic optical depth for the selected field of view.

1.6 Acknowledgments

The work detailed in this manuscript was supported by the National Science Foundation under Grant No. CBET-2022723. BMM and MW acknowledge support from the NorthEast Center for Chemical Energy Storage (NECCES), an Energy Frontier Research Center funded by the U.S. Department of Energy, Office of Science, Office of Basic Energy Sciences under award no. DE-SC0012583. This research used resources of the Advanced Photon Source; a U.S. Department of Energy (DOE) Office of Science user facility operated for the DOE Office of Science by Argonne National Laboratory under Contract No. DE-AC02-06CH11357. The Advanced Light Source is supported by the Director, Office of Science, Office of Basic Energy Sciences, of the U.S. Department of Energy under contract no. DE-AC02-05CH11231.

References

- (1) Srout, M.; El Kazzi, M.; Ben Youcef, H.; Fromm, K. M.; Saadoune, I. Improvement of the Electrochemical Performance by Partial Chemical Substitution into the Lithium Site of Titanium Phosphate-Based Electrode Materials for Lithium-Ion Batteries: LiNio.25Ti1.5 Fe0.5(PO4)3. J. Power Sources 2020, 461, 228114. https://doi.org/10.1016/j.jpowsour.2020.228114.
- (2) Velasco-Soto, M. A.; Licea-Jiménez, L.; Videa, M.; Martínez, L. M.; Morales-Sánchez, A.; Bautista-Carrillo, L. M.; Longoria-Rodríguez, F. E.; Castro-Pardo, S.; Esparza, S. G.; Rodríguez-Rodríguez, A. A.; Pérez-García, S. A. Improvement on Cell Cyclability of Lead–Acid Batteries through High-Energy Ball Milling and Addition of Multi-Walled Carbon Nanotubes in the Formulation of Leady Oxides. *J. Appl. Electrochem.* 2021, 51 (3), 387–397. https://doi.org/10.1007/s10800-020-01507-z.
- (3) Cao, X.; Li, H.; Qiao, Y.; Li, X.; Jia, M.; Cabana, J.; Zhou, H. Stabilizing Reversible Oxygen Redox Chemistry in Layered Oxides for Sodium-Ion Batteries. *Adv. Energy Mater.* **2020**, *10* (15), 1903785. https://doi.org/10.1002/aenm.201903785.
- (4) Tsai, P.-C.; Wen, B.; Wolfman, M.; Choe, M.-J.; Pan, M. S.; Su, L.; Thornton, K.; Cabana, J.; Chiang, Y.-M. Single-Particle Measurements of Electrochemical Kinetics in NMC and NCA Cathodes for Li-Ion Batteries. *Energy Environ. Sci.* 2018, 11 (4), 860–871. https://doi.org/10.1039/C8EE00001H.
- (5) Saito, T.; Nishikawa, K.; Nakamura, T.; Seki, S. Precise Analysis of Resistance Components and Estimation of Number of Particles in Li-Ion Battery Electrode Sheets Using LiCoO ₂ Single-Particle Electrochemical Properties. J. Phys. Chem. C 2020, 124 (31), 16758–16762. https://doi.org/10.1021/acs.jpcc.0c02881.
- (6) Woody, M.; Arbabzadeh, M.; Lewis, G. M.; Keoleian, G. A.; Stefanopoulou, A. Strategies to Limit Degradation and Maximize Li-Ion Battery Service Lifetime Critical Review and Guidance for Stakeholders. J. Energy Storage 2020, 28, 101231. https://doi.org/10.1016/j.est.2020.101231.
- (7) Xiong, R.; Ma, S.; Li, H.; Sun, F.; Li, J. Toward a Safer Battery Management System: A Critical Review on Diagnosis and Prognosis of Battery Short Circuit. iScience 2020, 23 (4), 101010. https://doi.org/10.1016/j.isci.2020.101010.
- (8) Wang, H.; Whitacre, J. F. Inhomogeneous Aging of Cathode Materials in Commercial 18650 Lithium Ion Battery Cells. *J. Energy Storage* **2021**, *35*, 102244. https://doi.org/10.1016/j.est.2021.102244.
- (9) Wolfman, M.; Yu, Y.-S.; May, B. M.; Lebens-Higgins, Z. W.; Sallis, S.; Faenza, N. V.; Pereira, N.; Shirato, N.; Rose, V.; Shapiro, D. A.; Amatucci, G. G.; Piper, L. F. J.; Cabana, J. Mapping Competitive Reduction upon Charging in LiNi _{0.8} Co _{0.15} Al _{0.05} O ₂ Primary Particles. *Chem. Mater.* 2020, 32 (14), 6161–6175. https://doi.org/10.1021/acs.chemmater.0c01986.

- (10) Hu, L.; Jokisaari, J. R.; Kwon, B. J.; Yin, L.; Kim, S.; Park, H.; Lapidus, S. H.; Klie, R. F.; Key, B.; Zapol, P.; Ingram, B. J.; Vaughey, J. T.; Cabana, J. High Capacity for Mg ²⁺ Deintercalation in Spinel Vanadium Oxide Nanocrystals. *ACS Energy Lett.* **2020**, *5* (8), 2721–2727. https://doi.org/10.1021/acsenergylett.0c01189.
- (11) Wolfman, M.; May, B. M.; Cabana, J. Visualization of Electrochemical Reactions in Battery Materials with X-Ray Microscopy and Mapping. *Chem. Mater.* **2017**, *29* (8), 3347–3362. https://doi.org/10.1021/acs.chemmater.6b05114.
- (12) Jung, R.; Morasch, R.; Karayaylali, P.; Phillips, K.; Maglia, F.; Stinner, C.; Shao-Horn, Y.; Gasteiger, H. A. Effect of Ambient Storage on the Degradation of Ni-Rich Positive Electrode Materials (NMC811) for Li-Ion Batteries. *J. Electrochem. Soc.* **2018**, *165* (2), A132–A141. https://doi.org/10.1149/2.0401802jes.
- (13) Garcia, J. C.; Bareño, J.; Yan, J.; Chen, G.; Hauser, A.; Croy, J. R.; Iddir, H. Surface Structure, Morphology, and Stability of Li(Ni _{1/3} Mn _{1/3} Co _{1/3})O ₂ Cathode Material. *J. Phys. Chem. C* **2017**, *121* (15), 8290–8299. https://doi.org/10.1021/acs.jpcc.7b00896.
- (14) Spingler, F. B.; Kücher, S.; Phillips, R.; Moyassari, E.; Jossen, A. Electrochemically Stable In Situ Dilatometry of NMC, NCA and Graphite Electrodes for Lithium-Ion Cells Compared to XRD Measurements. J. Electrochem. Soc. 2021, 168 (4), 040515. https://doi.org/10.1149/1945-7111/abf262.
- (15) Jung, R.; Metzger, M.; Maglia, F.; Stinner, C.; Gasteiger, H. A. Chemical versus Electrochemical Electrolyte Oxidation on NMC111, NMC622, NMC811, LNMO, and Conductive Carbon. *J. Phys. Chem. Lett.* **2017**, *8* (19), 4820–4825. https://doi.org/10.1021/acs.jpclett.7b01927.
- (16) Fan, Z.; Zhang, L.; Baumann, D.; Mei, L.; Yao, Y.; Duan, X.; Shi, Y.; Huang, J.; Huang, Y.; Duan, X. In Situ Transmission Electron Microscopy for Energy Materials and Devices. *Adv. Mater.* **2019**, *31* (33), 1900608. https://doi.org/10.1002/adma.201900608.
- (17) Shim, J.-H.; Kang, H.; Kim, Y.-M.; Lee, S. In Situ Observation of the Effect of Accelerating Voltage on Electron Beam Damage of Layered Cathode Materials for Lithium-Ion Batteries. *ACS Appl. Mater. Interfaces* **2019**, *11* (47), 44293–44299. https://doi.org/10.1021/acsami.9b15608.
- (18) Winarski, R. P.; Holt, M. V.; Rose, V.; Fuesz, P.; Carbaugh, D.; Benson, C.; Shu, D.; Kline, D.; Stephenson, G. B.; McNulty, I.; Maser, J. A Hard X-Ray Nanoprobe Beamline for Nanoscale Microscopy. *J. Synchrotron Radiat.* 2012, 19 (6), 1056–1060. https://doi.org/10.1107/S0909049512036783.
- (19) May, B. M.; Serrano-Sevillano, J.; Dauphin, A. L.; Nazib, A.; Lima, N.; Casas-Cabanas, M.; Cabana, J. Effect of Synthetic Parameters on Defects, Structure, and Electrochemical Properties of Layered Oxide LiNi _{0.80} Co _{0.15} Al _{0.05} O ₂. *J. Electrochem. Soc.* **2018**, *165* (14), A3537–A3543. https://doi.org/10.1149/2.1211814jes.
- (20) Zhang, H.; May, B. M.; Serrano-Sevillano, J.; Casas-Cabanas, M.; Cabana, J.; Wang, C.; Zhou, G. Facet-Dependent Rock-Salt Reconstruction on the Surface of Layered Oxide

- Cathodes. *Chem. Mater.* **2018**, *30* (3), 692–699. https://doi.org/10.1021/acs.chemmater.7b03901.
- (21) May, B. M.; Yu, Y.-S.; Holt, M. V.; Strobridge, F. C.; Boesenberg, U.; Grey, C. P.; Cabana, J. Nanoscale Detection of Intermediate Solid Solutions in Equilibrated Li_xFePO₄ Microcrystals. *Nano Lett.* **2017**, *17* (12), 7364–7371. https://doi.org/10.1021/acs.nanolett.7b03086.
- (22) Fujii, Y.; Miura, H.; Suzuki, N.; Shoji, T.; Nakayama, N. Structural and Electrochemical Properties of LiNi1/3Co1/3Mn1/3O2: Calcination Temperature Dependence. *J. Power Sources* **2007**, *171* (2), 894–903. https://doi.org/10.1016/j.jpowsour.2007.06.017.
- (23) Marchesini, S.; Krishnan, H.; Daurer, B. J.; Shapiro, D. A.; Perciano, T.; Sethian, J. A.; Maia, F. R. N. C. *SHARP*: A Distributed GPU-Based Ptychographic Solver. *J. Appl. Crystallogr.* **2016**, *49* (4), 1245–1252. https://doi.org/10.1107/S1600576716008074.
- (24) Judge, W.; Plews, M.; May, B.; Holt, M. V.; Cabana, J. Sxdm—A Python Framework for Analysis of Scanning X-Ray Diffraction Microscopy Data. *Softw. Impacts* **2021**, *10*, 100172. https://doi.org/10.1016/j.simpa.2021.100172.
- (25)Yoon, W.-S.; Chung, K. Y.; McBreen, J.; Yang, X.-Q. A Comparative Study on Structural Changes of LiCo1/3Ni1/3Mn1/3O2 and LiNi0.8Co0.15Al0.05O2 during First Charge Using in Situ XRD. *Electrochem. Commun.* **2006**, *8* (8), 1257–1262. https://doi.org/10.1016/j.elecom.2006.06.005.
- (26) Miao, S.; Kocher, M.; Rez, P.; Fultz, B.; Ozawa, Y.; Yazami, R.; Ahn, C. C. Local Electronic Structure of Layered $Li_xNi_{0.5}Mn_{0.5}O_2$ and $Li_xNi_{1/3}Mn_{1/3}Co_{1/3}O_2$. *J. Phys. Chem. B* **2005**, 109 (49), 23473–23479. https://doi.org/10.1021/jp0542266.
- (27) Kim, M. G.; Shin, H. J.; Kim, J.-H.; Park, S.-H.; Sun, Y.-K. XAS Investigation of Inhomogeneous Metal-Oxygen Bond Covalency in Bulk and Surface for Charge Compensation in Li-Ion Battery Cathode Li_xNi_{1/3}Co_{1/3}Mn_{1/3}O₂ Material. *J. Electrochem. Soc.* **2005**, *152* (7), A1320–A1328.
- (28) Mohanty, D.; Kalnaus, S.; Meisner, R. A.; Rhodes, K. J.; Li, J.; Payzant, E. A.; Wood, D. L.; Daniel, C. Structural Transformation of a Lithium-Rich Li1.2Co0.1Mn0.55Ni0.15O2 Cathode during High Voltage Cycling Resolved by in Situ X-Ray Diffraction. *J. Power Sources* **2013**, *229*, 239–248. https://doi.org/10.1016/j.jpowsour.2012.11.144.
- (29) Deng, C.; Zhang, S.; Fu, B. L.; Yang, S. Y.; Ma, L. Synthetic Optimization of Nanostructured Li[Ni_{1/3}Co_{1/3}Mn_{1/3}]O₂ Cathode Material Prepared by Hydroxide Coprecipitation at 273K. *J. Alloys Compd.* **2010**, *496* (1–2), 521–527. https://doi.org/10.1016/j.jallcom.2010.02.094.
- (30) Liu, X.; Wang, D.; Liu, G.; Srinivasan, V.; Liu, Z.; Hussain, Z.; Yang, W. Distinct Charge Dynamics in Battery Electrodes Revealed by in Situ and Operando Soft X-Ray Spectroscopy. *Nat. Commun.* **2013**, *4* (1), 2568. https://doi.org/10.1038/ncomms3568.

- (31) de Biasi, L.; Schwarz, B.; Brezesinski, T.; Hartmann, P.; Janek, J.; Ehrenberg, H. Chemical, Structural, and Electronic Aspects of Formation and Degradation Behavior on Different Length Scales of Ni-Rich NCM and Li-Rich HE-NCM Cathode Materials in Li-Ion Batteries. *Adv. Mater.* **2019**, *31* (26), 1900985. https://doi.org/10.1002/adma.201900985.
- (32) Ryu, H.-H.; Park, K.-J.; Yoon, C. S.; Sun, Y.-K. Capacity Fading of Ni-Rich Li[Ni $_x$ Co $_y$ Mn $_{1-x-y}$]O $_2$ (0.6 $\le x \le$ 0.95) Cathodes for High-Energy-Density Lithium-Ion Batteries: Bulk or Surface Degradation? *Chem. Mater.* **2018**, *30* (3), 1155–1163. https://doi.org/10.1021/acs.chemmater.7b05269.
- (33) Radin, M. D.; Hy, S.; Sina, M.; Fang, C.; Liu, H.; Vinckeviciute, J.; Zhang, M.; Whittingham, M. S.; Meng, Y. S.; Van der Ven, A. Narrowing the Gap between Theoretical and Practical Capacities in Li-Ion Layered Oxide Cathode Materials. *Adv. Energy Mater.* **2017**, *7* (20), 1602888. https://doi.org/10.1002/aenm.201602888.

TOC Graphic:

